Many-body quantum chaos and actinide ions: Testing the predictions of random matrix theory with high-Z ions

J. Sheil*
School of Physics, University College Dublin, Belfield, Dublin 4, Ireland

(Received 10 June 2018; published 31 August 2018)

In this study, we present a statistical analysis of the level structures of four highly charged actinide ions: Bk XII, Cf XII, No XIII, and Md XIV. In these ions, $5f$ wave-function contraction gives rise to a manifold of levels arising from configurations with partially filled $5f$ and $6p$ subshells. The cumulative effects of configuration interaction (CI) between these configurations results in a complete breakdown of the independent particle model used in the labeling of the states and leads to the formation of so-called "compound" states. Properties of the calculated level structures have been analyzed using the techniques of random-matrix theory (RMT). Standard statistical measures, such as the repulsion parameter q, the covariance of adjacent spacings $\mathrm{cov}(s_i, s_{i+1})$, and the Dyson-Mehta statistic $\Delta_3(L)$, have been computed for specific J^π interacting sets belonging to the four aforementioned ion stages. In the majority of cases, these calculations are found to be in very good agreement with the RMT-predicted values for these quantities. This study therefore extends previous identifications of RMT-like level fluctuations in the level spectra of lanthanide ions to high-Z, moderately charged actinide ions.

DOI: 10.1103/PhysRevA.98.022521

I. INTRODUCTION

Perhaps the most profound characteristic of Wigner's random matrix theory (RMT), aside from its mathematical elegance, is the powerful predictive capabilities of the theory in many seemingly unrelated fields of inquiry. Indeed, to date, RMT has found application in many diverse research topics. For example, in the field of mathematical finance, the tools of RMT have been utilized to quantify cross correlations between price fluctuations of stocks [1]. Another example arises in the field of acoustics, whereby the spectral statistics of acoustic resonances in aluminium and quartz blocks have been shown to be accurately described using RMT [2,3]. The ability of RMT to capture the universal features of these systems without knowledge of the underlying interactions is clearly quite remarkable, and this is what makes it an incredibly powerful tool. In the present study, the predicative capabilities of RMT in describing *gross* features of the level structures of highly charged actinide ions are studied. We wish to extend previous works on the level structure of the lanthanide ion Sm IX [4] to high-Z actinides ions.

RMT can trace its origins back to Eugene Wigner's work on the interpretation of nuclear spectra in the early 1950s [5]. The problem facing the nuclear community was to provide a quantitative understanding of the resonances observed in low-energy neutron scattering experiments from heavy nuclei (e.g., see Fig. 3 of [6]). In such systems, the incident neutron is captured by the nucleus, and its energy is shared among the constituent nucleons. Unfortunately, an accurate description of the excited states of these systems proved impossible using conventional nuclear theory of the time. Indeed, with increasing energy, the exponential increase in level density results in complicated level mixings and a complete breakdown in any approximate quantum numbers used in the description of the level structures. Because of these difficulties, accurate models of the underlying Hamiltonian proved impossible to construct.

The complicated, many-body nature of these interactions led Wigner to develop a statistical approach to the problem. In this method, one approximates a nuclear Hamiltonian by performing an averaging process over an ensemble of "model" Hamiltonian matrices, each of which share common symmetry properties. Importantly, to reflect the complicated nature of the interactions, each model Hamiltonian is populated with random variables drawn from some probability distribution. By performing the averaging process over a large ensemble of matrices, it is expected that the ensemble average should not deviate substantially from a true Hamiltonian [7,8]. It was surmised that the fluctuation properties of the eigenvalues of this Hamiltonian and those of the experimental level energies with equivalent "good" quantum numbers would be identical, and, furthermore, that the probability distribution of nearest-neighbor spacings (NNSs) s would be of the form

$$P(s) = \frac{\pi s}{2} \exp\left(\frac{-\pi s^2}{4}\right). \tag{1}$$

Remarkably, this distribution was found to reproduce experimental nuclear data magnificently, examples of which can be seen in [9]. In the years following this discovery, formal development of the mathematical underpinnings of the theory took hold. Dyson, for example, using group-theoretical results of Wigner, demonstrated the existence of three generic ensembles of random matrices: the Gaussian *orthogonal*, *unitary*, and *symplectic* ensembles [10]. Each ensemble is associated with a specific symmetry property of the Hamiltonian. GOE statistics, for example, are employed when describing nuclear (and atomic) Hamiltonians due to the time-reversal invariant nature of the system.

*john.sheil@ucdconnect.ie

Given the overwhelming evidence of GOE-like behavior in the spectra of nuclear scattering systems, it is natural to ask whether RMT-like behavior could be observed in the spectra of atomic systems. Rosenzweig and Porter [11] addressed this problem by undertaking a comprehensive examination of the level structures of atoms and ions belonging to the third, fourth, and fifth rows of the Periodic Table. Interestingly, Wigner's prediction (1) was found to mirror the level distribution of sets with equivalent good quantum numbers belonging to the fifth row of the Periodic Table, an observation attributed to the increasing strength of spin-dependent forces as one moves to the fifth row. In the atomic case, good quantum numbers correspond to the total angular momentum J and the parity π, and a group of levels with equivalent J^π labels is known as an *interacting set*. More than 20 years later, Camarda and Georgopolous [12], using energy-level data compiled by Martin, Zalubas, and Hagan [13], identified energy-level fluctuations in the level spectra of lanthanide ions consistent with the predictions of the GOE.

Since the 1980s, numerous studies have examined the role of RMT in describing complex atomic systems. Flambaum *et al.* [14], inspired by the work of Chirikov [15], performed a comprehensive study on the structure of the eigenstates of neutral cerium. The presence of several low-lying orbitals ($4f$, $6s$, $5d$, and $6p$) was found to generate an enormous level density. In fact, the average level spacing D was found to be significantly smaller than the off-diagonal residual interaction $V = \langle \Phi_i | H | \Phi_j \rangle$, resulting in a complete breakdown of the independent particle model ($V/D \gg 1$). As before, only good quantum numbers, i.e., J^π, are useful in the labeling of levels. The eigenstates of the system were found to be built from a random or chaotic superposition of a large number of basis states (number of principal components $N_{\rm eig} \approx 70$), hence the term *many-body quantum chaos*.

Although neutral Ce provides a very suitable testing ground for the identification of many-body quantum chaos, it is interesting to ask whether values for $N_{\rm eig}$ similar to those encountered in the nuclear case ($N_{\rm eig} \approx 10^4$–10^6) can be found in other atomic systems. O'Sullivan and co-workers [16,17] have identified such a system: lanthanide ions in the presence of $4f$ wave-function collapse [18]. Briefly, the double-well nature of the $4f$ potential is such that, in the neutral lanthanides, the centrifugal term in the radial potential dominates and the $4f$ eigenfunction is located in the outer well [18–20]. However, with increasing ionization, the strength of the attractive nuclear Coulomb term becomes dominant, and the repulsive barrier separating the outer and inner wells drops, resulting in contraction of the $4f$ wave function towards the core [21,22]. In the process of $4f$ wave-function contraction, configurations with variable $4f/5s/5p$ occupancy overlap significantly in energy, resulting in an enormous level density and a complete breakdown of any independent electron designations. Indeed, recent calculations, building on the experimental work of Carroll and O'Sullivan [23] and O'Sullivan [24], have identified an admixture of $4f/5p$ and $4f/5s$ electrons in the ground-state configurations of moderately charged lanthanide ions [25]. Clearly, these structures adhere to the requirements of a system exhibiting many-body quantum-chaotic features. To investigate whether such structures do indeed exhibit quantum chaotic features, Kilbane *et al.* [4] have undertaken a comprehensive analysis of the eigenstates and eigenvalues associated with even- and odd-parity states of Sm IX. Strong evidence of quantum chaotic features were found to prevail in the energy-level statistics of odd Sm IX. Interestingly, behavior intermediate between the regular and chaotic extremes was identified for even Sm IX.

In terms of postlanthanides, we know of only one study, that of Viatkina *et al.* [26], which has examined many-body quantum chaotic signatures in high-Z species. Chaotic behavior in the spectrum of neutral Pa was identified by examining the level structures and eigenstates of numerous J^π interacting sets, as well as the observation of a statistical enhancement of small perturbations *via* the three-electron interaction of valence electrons. In the present work, we have extended the identification of many-body quantum chaos from neutral Pa to moderately charged actinide ions. Indeed, in a recent calculation of the ground-state configurations of actinide ions [27], the effects of $5f$ wave-function contraction were found to be significant and lead to strong competition between the $5f$ and $6p$ electrons in the formation of the ground states. Naturally, because of the highly correlated nature of these level structures, the question of whether such systems exhibit chaotic features was addressed. As a test case, the level structure of the $J^\pi = 5^+$ interacting set in Rn-like Cm (Cm^{10+}) was examined.

Indeed, this level sequence was found to be extremely dense. Moreover, a striking similarity between the level distribution of this interacting set and that calculated using Wigner's prediction (1) was observed.

An extension of this work has been undertaken in the present study, whereby we have perfomed more elaborate RMT tests on the level structures of numerous actinide ions. These tests have been performed on ion stages exhibiting a pronounced contraction of the $5f$ wave function, i.e., significant $5f/6p$ wave-function overlap. Short- and long-range correlations in the spectra have been identified by evaluating quantities such as the repulsion parameter q, the covariance of adjacent spacings $\mathrm{cov}(s_i, s_{i+1})$, and the Dyson-Mehta statistic $\Delta_3(L)$. Direct comparisons have been made with the RMT-predicted values for these quantities, thus allowing for the quantification of RMT's suitability in describing *gross* features of the level structures.

The structure of the present paper is as follows. In Sec. II, we describe the underlying theoretical method and computational procedure adopted in the flexible atomic code (FAC) [28] for the calculation of the level structures. In Sec. III the results of a comprehensive statistical study on the level structures are presented. Finally, we conclude with a summary of the present work in Sec. IV.

II. ATOMIC STRUCTURE CALCULATIONS

A standard technique often used to identify quantum chaotic signatures in atoms and/or ions involves performing statistical tests on detailed, accurate energy-level "data sets." Here, each data set corresponds to a well-defined J^π manifold of interacting energy levels, where, importantly, each J^π manifold is treated independent of the other manifolds. In this regard, one possible approach would involve performing these statistical tests on experimentally obtained energy levels, as

was demonstrated by Rosenzweig and Porter in their pioneering work of 1960 [11]. However, the trade-off between the intrinsic complexity of the level sequences and the preciseness required when assigning accurate J^π labels typically results in a series of fragmentary J^π manifolds (e.g., see [11]). In such cases, the appropriateness of applying statistical tests is questioned. Moreover, the obvious overarching restriction to this approach is simply a lack of experimental level structure data, which, unfortunately, applies here in the case of highly charged actinide ions.

In light of the above considerations, we are clearly restricted to performing these statistical tests on accurate theoretical calculations of the level structures. For the ions considered in this work, accurate calculations of the level structures require the simultaneous, detailed treatment of both relativistic and correlation effects. A technique often used in such situations involves modeling the atomic-ionic structure using the Dirac-Fock-Slater approach implemented in the flexible atomic code (FAC) [28]. To date, the FAC has proven to be a powerful tool for reproducing accurate atomic radiative and collisional quantities such as energy levels, transition rates, autoionization rates, photoionization cross sections, etc. It is a flexible, versatile code, which, in its design, has built on the strength of existing codes, such as HULLAC [29] and the Pennsylvania code developed by Sampson *et al.* [30,31].

In the FAC, the level structure is built from an underlying N-electron Dirac-Coulomb Hamiltonian

$$H = \sum_{i=1}^{N}\left[(\boldsymbol{\alpha_i}.\boldsymbol{p_i})c + (\beta_i - 1)c^2 - \frac{Z}{r_i}\right] + \sum_{i<j}^{N}\frac{1}{r_{ij}}, \qquad (2)$$

where c is the speed of light and $\boldsymbol{\alpha_i}$, β_i are the Dirac matrices. The (approximate) atomic state functions (ASFs) $|\Psi(JM_J\pi)\rangle$ of the system are represented as a linear combination of configuration state functions (CSFs) $|\Phi(JM_J\pi)\rangle$ of the same symmetry

$$|\Psi(JM_J\pi)\rangle = \sum_k c_k|\Phi_k(JM_J\pi)\rangle, \qquad (3)$$

where the expansion coefficients c_k are obtained through diagonalization of the Hamiltonian. Each individual CSF in the summation (3) is written as a Slater determinant of N one-electron Dirac spinors φ, where, in the relativistic formalism, φ is written

$$\varphi_{n\kappa m} = \frac{1}{r}\begin{bmatrix} P_{n\kappa}(r)\chi_{\kappa m}(\theta,\phi,\sigma) \\ iQ_{n\kappa}(r)\chi_{-\kappa m}(\theta,\phi,\sigma)\end{bmatrix}. \qquad (4)$$

Here, n is the principal quantum number, m is the magnetic quantum number for a single-electron orbital, and $\kappa = (l-j)(2j+1)$ is the relativistic angular momentum quantum number. The functions $\chi_{\kappa m} = \sum_{m_l,m_s} C(l\tfrac{1}{2}m_l m_s; jm)Y_{lm_l}(\theta,\phi)\delta(m_s|\sigma)$ are the standard spin-angular functions, $\delta(m_s|\sigma)$ are the spin functions, and the quantities $P_{n\kappa}(r)$ and $Q_{n\kappa}(r)$ are the *large* and *small* components of the radial wave function, respectively.

The first step in any atomic structure computation is the accurate calculation of the radial orbitals. In the Dirac-Fock-Slater method pursued here, the components $P_{n\kappa}(r)$ and $Q_{n\kappa}(r)$ satisfy the following coupled Dirac equations:

$$\left(\frac{d}{dr} + \frac{\kappa}{r}\right)P_{n\kappa}(r) = \alpha\left(E_{n\kappa} - V(r) + \frac{2}{\alpha^2}\right)Q_{n\kappa}(r), \qquad (5)$$

$$\left(\frac{d}{dr} - \frac{\kappa}{r}\right)Q_{n\kappa}(r) = \alpha[-E_{n\kappa} + V(r)]P_{n\kappa}(r), \qquad (6)$$

where $\alpha \approx 1/137$ is the fine-structure constant, the energy eigenvalues of the radial orbitals are written $E_{n\kappa}$, and the local central potential is given by $V(r)$. Although not provided here, the expression for $V(r)$ used in the FAC is a summation over all subshells $n\kappa$ involving the terms $P_{n\kappa}$ and $Q_{n\kappa}$. Because of this interdependency $[V(r) \leftrightarrow P_{n\kappa}, Q_{n\kappa}]$, one solves (5) and (6) for the components $P_{n\kappa}$ and $Q_{n\kappa}$ self-consistently.

In the FAC, a single local central potential $V(r)$ is used throughout the calculations. A straightforward derivation of $V(r)$ would involve summing over all $n\kappa$ subshells of the ground-state configuration. In this approach, only a single configuration is used to optimize the radial potential. In the case of excited-state configurations, however, this potential is clearly less well suited. As a compromise, the approach adopted in the FAC is to optimize this radial potential using a "fictitious" configuration with fractional occupation numbers. The purpose of this fictitious configuration is to best reflect the influence of both the ground- and excited-state configurations in a single optimization of the radial potential. For example, a fictitious configuration for a Ne-like ion (ground-state configuration $1s^22s^22p^6$) could take the form $1s^22s^22p^43s^13p^{0.6}3d^{0.4}$. This approach was first adopted in the codes of Sampson *et al.* [30,31] and has been used to great effect to generate accurate, reliable level structure data. The choice of occupancy weighting in this fictitious configuration, however, is clearly quite arbitrary, and caution is therefore needed in its construction. For example, as mentioned by Gu [28], the inclusion of high-lying orbitals in this fictitious configuration may lead to a more diffuse radial potential than actually exists in the physical system, thus leading to inaccurate level structure data. In order to correct for the use of this less-optimized potential, the FAC implements a correction to the original procedure. In the first step, the average energies of each configuration adopted in the model are calculated using radial potentials optimized to each individual configuration. Next, the radial potential is optimized using a single fictitious configuration, and the average energy of each configuration is recalculated using this less-optimized potential. Construction of the Hamiltonian matrix follows suit. Finally, before explicit diagonalization of the Hamiltonian matrix, one adds as a correction to the appropriate Hamiltonian matrix elements the differences in configuration average energies calculated using the optimized and less-optimized potentials.

As highlighted in the Introduction, we have recently undertaken a calculation [27] of the ground-state configurations of actinide ions in charge states VII–XXV using the pseudorelativistic and fully relativistic approaches implemented in the Cowan code [32] and the FAC [28], respectively. We have adopted the results of the FAC level structure calculations in the current study. As a reminder, calculations of the charge state structures of isoelectronic sequences in the range Au-like to Rn-like were performed with variable numbers of

TABLE I. Charge states, interacting sets, configurations included in the calculations, and the range of J values considered in the calculations.

Ion stage	J^π	Configurations	J
Bk XII	3^+	$5f^8, 5f^7 6s, 5f^6 6s^2, 5f^5 6p, 5f^4 6p^2$ $5f^3 6p^3, 5f^2 6p^4, 5f 6p^5, 6p^6$	$0 \rightarrow 13$
Cf XII	$\frac{7}{2}^-$	$5f^7, 5f^6 6p, 5f^5 6p^2$ $5f^4 6p^3, 5f^3 6p^4, 5f^2 6p^5, 5f 6p^6$	$\frac{1}{2} \rightarrow \frac{27}{2}$
No XIII	4^+	$5f^{10}, 5f^9 6p, 5f^8 6p^2$ $5f^7 6p^3, 5f^6 6p^4, 5f^5 6p^5, 5f^4 6p^6$	$0 \rightarrow 15$
Md XIV	3^+	$5f^8, 5f^7 6p, 5f^6 6p^2$ $5f^5 6p^3, 5f^4 6p^4, 5f^3 6p^5, 5f^2 6p^6$	$0 \rightarrow 14$

$5f/6s/6p$ occupancy, i.e., all possible configurations of the form $5f^n 6s^k 6p^m$ were included in the calculations, where $n+k+m$ is the number of electrons additional to a Pt-like core (outermost subshell of the form $5d^{10}$). Here, the occupation numbers n, k, and m are integers. For the heavier isoelectronic sequences in the range Fr-like to Bk-like, only configurations with variable $5f/6p$ occupancy were considered. This choice of reduced configuration space is justified, however, since the $5f$ binding energy only overtakes the $6s$ at ion stages well in excess of the moderately charged states considered here. For example, in the Rn-like isoelectronic sequence, $5f/6s$ level crossing was shown to occur near the 36th ion stage ($Z \approx 121$) [27]. A detailed list of configurations included in the calculations along with the range of J values considered in these calculations are presented in Table I. As noted in this study, the construction of a fictitious configuration for the optimization of the radial potential is significantly difficult given the existence of strong CI in the system and also a lack of experimental data to which to compare the calculated level structures. To circumvent this difficulty, two sets of calculations were performed for each ion stage, whereby the fictitious configuration used corresponded to (i) the configuration associated with the lowest-lying level and (ii) the next lowest-lying configuration. Both sets of calculations consistently yielded the same ground-state configurations. For the current study, we will adopt the level structures calculated using the first approach. Although we are dealing with high-Z ions, higher-order corrections to the Hamiltonian, such as the Breit interaction, were not included in the original calculations. This decision was built on the premise that the electron-electron interactions, described through the Slater integrals F^k, G^k and the Slater CI integrals R^k, would dominate over higher-order effects. Indeed, the Breit correction to the interaction between valence electrons is on the order of α^2, significantly smaller than the interactions described above [33]. However, as discussed by Kozlov *et al.* [33], the Breit correction to the exchange interaction between the valence electrons and the core electrons is typically non-negligible.

In order to examine this further, we wish to compare the results of level structure calculations performed both with and without the Breit interaction included in the Hamiltonian. To do so, we have examined the $J^\pi = 3^+$ interacting set in the Bk XII ion.

Let $E_{n,\text{Breit}}$ denote the nth level calculated with the inclusion of the Breit interaction and E_n denote the nth level calculated without this perturbation. The standard procedure for quantifying the strength of such a pertubation involves identifying equivalent levels in both sets of calculations and comparing their calculated energies. This identification is typically done by identifying levels with identical quantum numbers. If the corrections to the energies are rather small and if the level structures are not too dense, one can simply match levels based on the ordering of their energies, i.e., $E_{1,\text{Breit}} \Leftrightarrow E_1$, $E_{2,\text{Breit}} \Leftrightarrow E_2$, etc.

Unfortunately, the process of matching levels with identical quantum numbers is extremely difficult in the case of dense level structures. Indeed, the existence of numerous near-equally weighted basis states contributing to each level makes the labeling of these levels via the leading eigenvector rather ambiguous. The corresponding expansion coefficients of these basis states are highly sensitive to variations in the Hamiltonian matrix elements. Therefore, the introduction of a perturbation into the Hamiltonian, such as the Breit interaction, can alter these expansion coefficients and cause a redesignation of a level according to the new leading eigenvector. This feature is evident in the level structure of the $J^\pi = 3^+$ interacting set.

In order to quantify the deviations between both calculations, we first order the levels in terms of increasing energies as outlined above. The deviation between two levels is then obtained from the statistic $\gamma = 100 \times |E_{n,Breit} - E_n|/E_n$. Interestingly, this statistic takes on its largest values for levels below 20 eV ($0.4\% < \gamma < 7.6\%$). However, as one moves to higher excitation energies, γ tends to converge around a value of 1%. Clearly, the inclusion of this perturbation does not have a significant influence on the general level structure. Although the level labels may change, the $J^\pi = 3^+$ level structure varies only slightly. Therefore, it is the eigenvectors rather than the eigenvalues that are most affected by the inclusion of the Breit interaction in the Hamiltonian. Given that the statistical tests only depend on the level structures, we conclude that the neglection of the Breit interaction in the level structure calculations should not have a significant influence on the outcome of the RMT statistical tests.

III. LEVEL STRUCTURES AND RMT STATISTICS

In the present section, we introduce and describe the numerous statistical tests we have performed on the level structures. This will enable us to identify the existence of short- and long-range correlations in the energy-level spectra. As mentioned by Dyson [10], it is important to note that the goal of Wigner's statistical theory is to best reproduce *gross* features of the spectrum, such as the distribution of spacings between adjacent levels. Localized quantities, such as the ordering of levels, cannot be reproduced by the theory.

A. Criteria for selection of ion stages and J^π sets

The appropriate choice of ion stage and J^π interacting set is a key step in the identification of many-body quantum chaos in an atomic-ionic system. As already discussed, the vital component of such a system exhibiting GOE statistics is that there must be some form of breakdown of the shell

TABLE II. Charge states, interacting sets, N_{total}, and N_{studied}.

Ion stage	J^π	N_{total}	N_{studied}
Bk XII	3^+	615	109
Cf XII	$\frac{7}{2}^-$	1121	162
No XIII	4^+	2468	104
Md XIV	3^+	1627	86

structure. Any approximate symmetries, such as those described through the quantum numbers n, L, or S, must be destroyed. The level structure must be extremely dense in nature and display strong configuration mixing ($V/D \gg 1$). In this sense, systems which contain well-defined bands of levels ascribed to a single configuration, well-separated in energy from neighboring configurations, are not useful for the current purposes. An examination of the level structures calculated in [27] has identified the lightly ($q+ < 5+$) and heavily ($q+ > 16+$) ionized species as having relatively ordered level structures. In the case of the former, the $5f$ wave function is an eigenstate of the outer well and has not undergone significant contraction into the inner well region. No significant disruption of level orderings has therefore occurred for these species. In the case of highly charged ions, the $5f$ wave function has fully contracted into the inner region, and ground-state configurations typically take the form $5f^n$. Although partial overlap with neighboring configurations is observed (due to the large energy spread of $5f^n$ configurations), well-defined energy-dependent configuration bands still emerge in these systems. The natural testing ground for the current study therefore lies between the two extremes mentioned above. In the case of moderately charged actinide ions, $5f$ wave-function contraction results in significant $5f/6p$ wave-function overlap. As a result, configurations with variable $5f/6p$ occupancy overlap in energy, and the strong interactions and extremely dense level structures in these systems result in a complete breakdown of any independent electron designations.

Now that the range of testable charge states has reduced, the next step involves identifying appropriate J^π interacting sets on which to perform the statistical tests. The criterion adopted here is that each interacting set must contain a significantly large number of levels. In the case of the four interacting sets chosen here, each J^π group contains >600 levels. However, as mentioned in the next section, statistical tests are typically performed on subsections of an interacting set. Accounting for this restriction, we have chosen regions of the energy spectra which contain no fewer than 80 levels. Information regarding the four chosen ion stages, the interacting sets, and the number of levels in (i) the entire energy region N_{total} and (ii) the studied energy region N_{studied} is provided in Table II. Energy-level diagrams belonging to the four ion stages are presented in Figs. 1–4 . The energy levels shown in these plots belong to all possible J^π sets. In these plots, the level spectra are given a constant height on the y axis. Superimposed on top of each plot, shown in red, is a histogram of the level density. More specifically, the height of each histogram bin corresponds to the ratio of the number of energy levels contained within that bin to the total number of energy levels in the spectrum. The level structures are clearly very

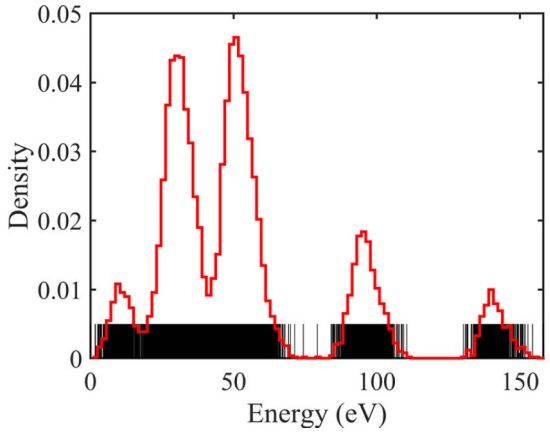

FIG. 1. Energy-level diagram of Bk XII. Superimposed on top of the energy-level spectrum, shown in red, is the energy-level density (see text for description).

dense, and each ion stage exhibits an interesting variation of level density with excitation energy. In Fig. 5 we illustrate the energy spectra of the four interacting sets considered in the present work. Energy levels enclosed within the red boxes were utilized in the present study.

B. Level densities and cumulative level distributions

Calculations performed with the FAC provide a sequence of eigenvalues which we shall denote by the set $\{E_1, E_2, E_3, \ldots, E_n\}$, where $E_1 < E_2 < E_3 < \cdots < E_n$. Throughout these calculations, the ground level is fixed at $E_1 = 0$ eV. The level structure is described through the level density $\rho(E)$, where

$$\rho(E) = \sum_{i=1}^{n} \delta(E - E_i). \tag{7}$$

A quantity often used in the description of level structure is the *mode number* or *cumulative level distribution* $N(E)$. It

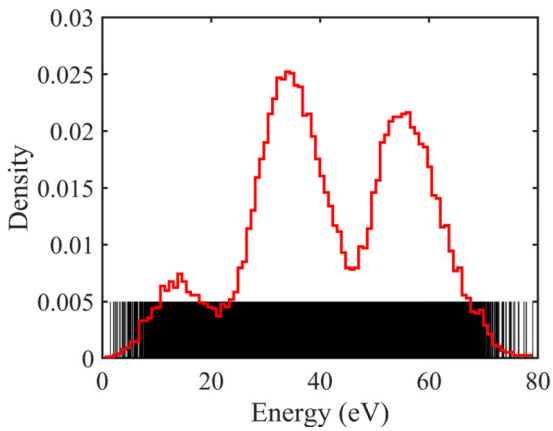

FIG. 2. Energy-level diagram of Cf XII. Superimposed on top of the energy-level spectrum, shown in red, is the energy-level density (see text for description).

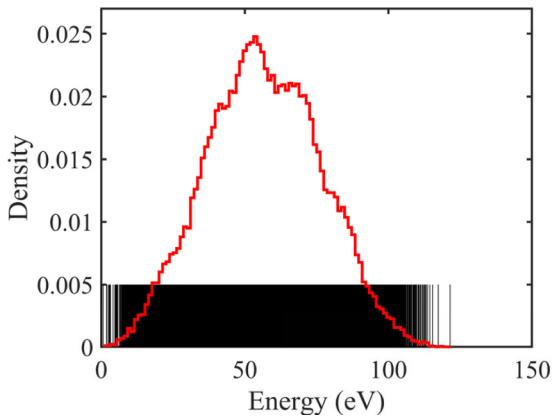

FIG. 3. Energy-level diagram of No XIII. Superimposed on top of the energy-level spectrum, shown in red, is the energy-level density (see text for description).

is written

$$N(E) = \sum_{i=1}^{n} \Theta(E - E_i). \tag{8}$$

$N(E)$ counts the number of levels with energies up to and including E, and is related to the level density through $N(E) = \int \rho(E')dE'$. A plot of $N(E)$ versus E takes on the appearance of a staircase and reveals changes in the level density as a function of excitation energy. This quantity is shown in Figs. 6 and 7 for the $J^\pi = 7/2^-$ and 4^+ interacting sets in Cf XII and No XIII, respectively. First, it is important to note the enormous level densities associated with these interacting sets. In each case, there are over 1100 and 2400 levels below 80 and 120 eV, respectively (see Table II). In the case of the $J^\pi = 7/2^-$ interacting set, significant changes in level density are observed across the entire energy range. Two regions of the spectrum exhibit an almost linear dependence of the mode number on excitation energy (31 → 40 and 52 → 58 eV). A reduction in the level density is observed between these two regions. This behavior can be attributed to the fluctuating level density observed in Fig. 2. Indeed, the coupling of three (or more) $5f$ electrons gives rise to three bands of levels, each separated by regions of small level densities. Increasing the number of $5f$ electrons results in these bands becoming less distinctive because of the large number of levels associated with these configurations. Indeed, the irregular behavior of the mode number in the region below 30 eV of Fig. 6 may also be attributed to this behavior.

From the above discussion, one can conclude that the level spectrum in the 0–70 eV region of the $J^\pi = 7/2^-$ interacting set exhibits a pronounced *nonuniformity* in its level density. It is impossible to define a single mean level density for the energy range. The first step therefore in any statistical analysis of a level sequence is to remove this energy-dependent density and to perform what is known as *unfolding*. In this procedure, one transforms the level distribution into one with unit level density, i.e., one rescales the energy levels such that, on average, each level is separated from its neighboring levels by a unit of 1. To do so, an appropriate region of the level spectrum is chosen, and a curve, denoted $\bar{N}(E)$ (known as the mean mode number), is fitted to the data. An example of this can be seen in Fig. 8, where we have chosen the 52.004 →

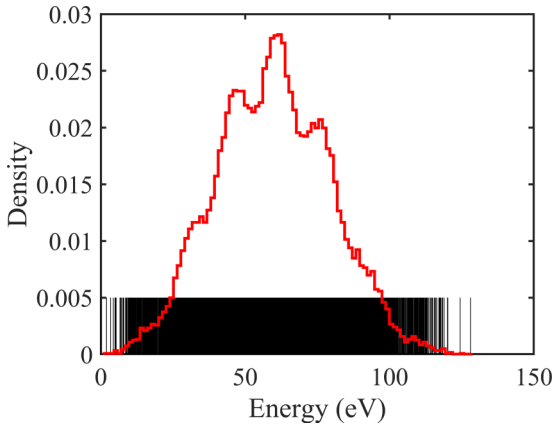

FIG. 4. Energy-level diagram of Md XIV. Superimposed on top of the energy-level spectrum, shown in red, is the energy-level density (see text for description).

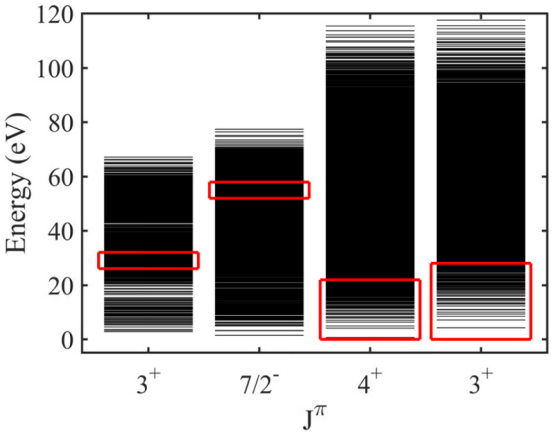

FIG. 5. Energy-level spectra of the four J^π sets: 3^+ (Bk XII), $7/2^-$ (Cf XII), 4^+ (No XIII), and 3^+ (Md XIV). The red boxes superimposed on top of the level spectra indicate the regions where the spectra were unfolded (see text and Table II).

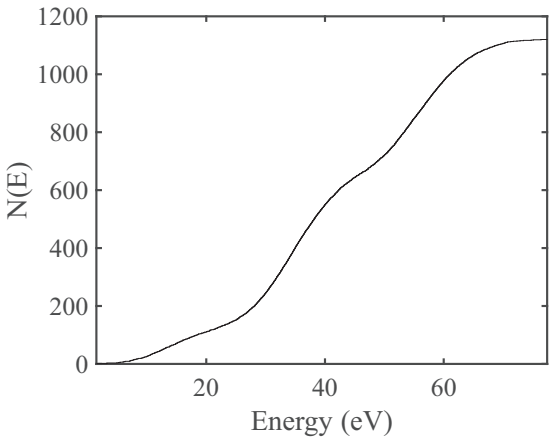

FIG. 6. Mode number $N(E)$ as a function of energy for the $J^\pi = 7/2^-$ interacting set in Cf XII.

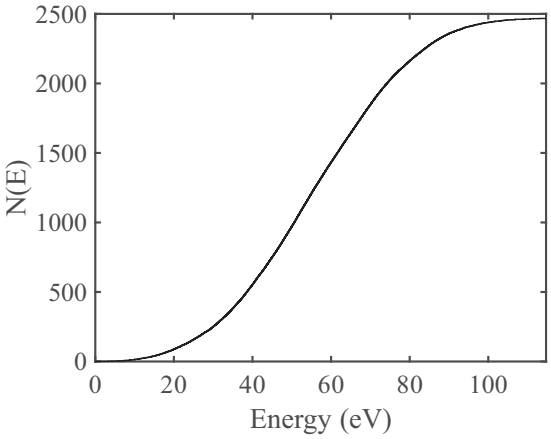

FIG. 7. Mode number $N(E)$ as a function of energy for the $J^\pi = 4^+$ interacting set in No XIII.

57.9907 eV region of Fig. 6 and have performed a single-order polynomial least-squares fit to the data. The line of best fit, $\bar{N}(E)$, is shown in red and reproduces the level structure data to a high accuracy. This is demonstrated quantitatively by an R-square value of 0.9998 [Here, the R-square value is defined as the ratio of the sum of squares of the regression (SSR) to the addition of the sum of squares of the error (SSE) and the SSR, i.e., $R^2 = \mathrm{SSR}/(\mathrm{SSE} + \mathrm{SSR})$. An R-square value close to 1 indicates an accurate fit to the data.] Furthermore, this region of the spectrum has the advantage of a large number of interacting levels ($N_{\mathrm{studied}} = 162$). Using the mean mode number, it is possible to define a new energy scale as the quantity $\bar{N}(E)$ evaluated at the original level energies, i.e., $\epsilon_j = \bar{N}(E_j)$. The new unfolded energies, therefore, belong to the set $\{\bar{N}(E_1), \bar{N}(E_2), \bar{N}(E_3), \ldots, \bar{N}(E_n)\}$. In order to demonstrate that this sequence has unit level density, first observe that the original staircase function $N(E)$ could be written as a combination of a smooth, "average" part $N_{\mathrm{av}}(E) = \bar{N}(E)$ (the best fit line) plus a fluctuating component $N_{\mathrm{fluc}}(E)$,

$$N(E) = N_{\mathrm{av}}(E) + N_{\mathrm{fluc}}(E). \tag{9}$$

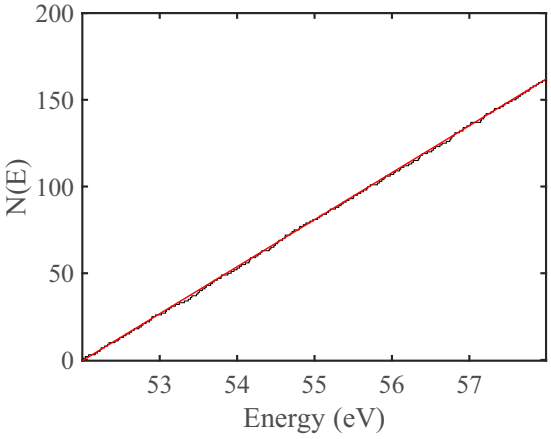

FIG. 8. Mode number $N(E)$ as a function of energy for the 52.0004 → 57.9907 eV range of Fig. 6. The mean mode number is shown in red.

Because we are solely interested in studying the fluctuation properties of the sequence, the $N_{\mathrm{av}}(E)$ dependence in the mode number must be removed. Defining the new energy scale as $\epsilon = \bar{N}(E)$, we observe that $\epsilon = N_{\mathrm{av}}(\epsilon)$. Therefore, the average level density, $\rho_{\mathrm{av}}(\epsilon) = dN_{\mathrm{av}}(\epsilon)/d\epsilon$, is equal to unity. The mode number of this sequence is described through

$$\hat{N}(\epsilon) = \epsilon + \hat{N}_{\mathrm{fluc}}(\epsilon), \tag{10}$$

where the level fluctuations have been rescaled in accordance with the new level density of unity.

A single-order polynomial least-squares fitting procedure has also been performed for the 26.0873 → 31.9287 eV energy region of the $J^\pi = 3^+$ interacting set in Bk XII. Apart from a reduction in the number of levels in the interacting set, the unfolding procedure performed for this set was identical to that for the $J^\pi = 7/2^-$ case. As before, excellent agreement between $\bar{N}(E)$ and $N(E)$ is illustrated by an R-square value of 0.9991.

Depending on the shape of the level distribution, there exists numerous ways to fit a curve to $N(E)$. In the examples explored above, a single-order polynomial was used in the least-squares optimization procedure because of the strong linear dependence of the level density on excitation energy. As one might expect, however, the choice of a linear fitting function is not always appropriate. Indeed, an exponential increase in level density is typically observed when moving from low-lying levels located near the ground level to higher excitation energies. An example of this behavior can be seen in Fig. 7 for the $J^\pi = 4^+$ interacting set in No XIII. A standard method to model such behavior involves adopting the independent particle model expression for $\rho(E)$ [12,34] and fitting the following curve to $N(E)$:

$$\bar{N}(\rho_0, a, E) = \int_{E_l}^{E} \rho_0 \exp(a\sqrt{E' - E_l})dE'. \tag{11}$$

Here, ρ_0 and a are curve fitting parameters and E_l is the energy of the lowest-lying level of the interacting set. Evaluating this integral one obtains

$$\bar{N}(\rho_0, a, E) = \frac{2\rho_0}{a^2}[\exp(a\sqrt{E - E_l})(a\sqrt{E - E_l} - 1) + 1]. \tag{12}$$

Using this equation, we have studied the low-energy regions of the $J^\pi = 4^+$ and 3^+ interacting sets in No XIII and Md XIV, respectively. For simplicity, the energies of these interacting sets have been rescaled such that $E_l = 0$ eV. In Fig. 9, the fit of (12) to the mode number $N(E)$ for the $J^\pi = 4^+$ set is illustrated. Excellent agreement of this fit to the data is illustrated by an R-square value of 0.9996. Similar agreement is observed for the $J^\pi = 3^+$ case in Md XIV ($R^2 = 0.9992$). Good agreement of the fit $\bar{N}(E)$ to the data $N(E)$ is vital in order for the statistical tests to be applied on accurate rescaled energy levels (unfolded energy levels). Values of ρ_0 and a obtained from the fit (12) to the data for these two interacting sets are presented in Table III.

It is important to note that, for the remainder of this study, all statistical tests will be performed on the unfolded energy scales $\bar{N}(E_j) = \epsilon_j$. Finally, we define the so-called nearest-neighbor spacing (NNS) s_j as $s_j = \bar{N}(E_{j+1}) - \bar{N}(E_j)$.

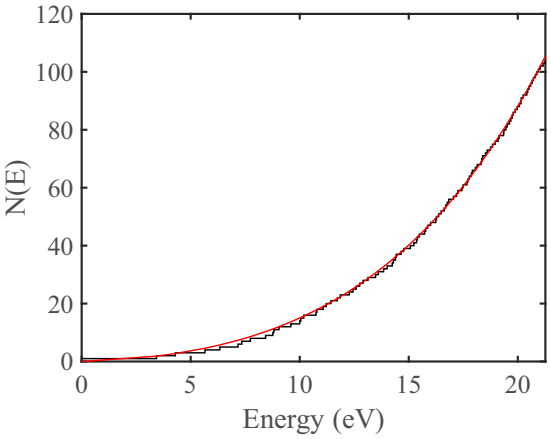

FIG. 9. Mode number $N(E)$ as a function of energy for the $0.6929 \rightarrow 21.9582$ eV range of Fig. 7. The energy levels associated with this range have been rescaled such that the lowest level has an energy of 0 eV. The mean mode number is shown in red.

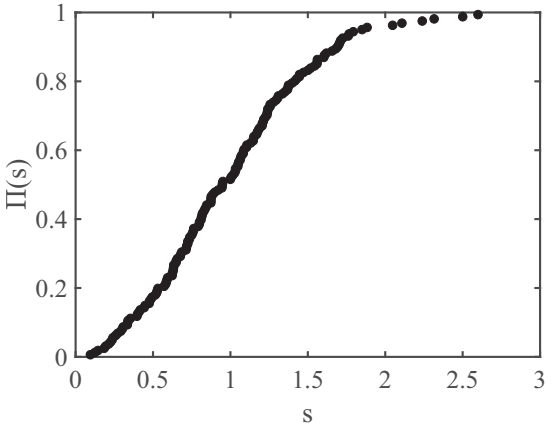

FIG. 10. Cumulative spacing distribution $\Pi(s)$ as a function of NNS's s for the $J^\pi = 7/2^-$ interacting set in Cf XII.

C. Brody parameters and nearest-neighbor spacing distributions

One of the characteristic features of a many-body quantum chaotic system is the existence of so-called *level repulsion*. Indeed, it is a fundamental property of quantum theory that two levels belonging to the same interacting set cannot be degenerate if they are coupled by nonzero matrix elements [35]. In effect, the levels "repel" each other.

This repulsive nature is inherent to Eq. (1), where it can be seen that the probability of finding two close-lying levels vanishes as $s \rightarrow 0$. Therefore, it is perhaps no surprise that the level distributions of highly correlated, dense atomic-ionic level structures are, generally, well described using Eq. (1).

In the opposite case, where one is faced with a system of uncorrelated levels belonging to independent J^π manifolds, there is no restriction on degeneracy. In this case, the distribution of NNSs follows a Poisson distribution [recall $P(s) \propto e^{-s}$], and near degeneracies are a common occurrence. In terms of a single J^π manifold, the existence of any nonzero off-diagonal matrix elements V destroys any possibility of level degeneracies, and Poisson-like statistics cannot emerge. This behavior was observed in a study of Sm IX carried out by O'Sullivan *etal*. [16], whereby Poisson-like statistics were observed in the NNS distribution of level structures calculated in the absence of CI. Moreover, inclusion of CI forced a Wigner-like distribution of NNSs.

In the vast majority of systems, however, it is rare that the level statistics follow precisely either of the two extremes mentioned above. Instead, behavior intermediate to these two cases is typically observed. In order to quantify the degree of intermediacy, one uses the so-called *Brody distribution* [36,37], given by

$$P_q(s) = \alpha(q+1)s^q \exp(-\alpha s^{q+1}). \tag{13}$$

Here, $\alpha = [\Gamma(\frac{q+2}{q+1})]^{q+1}$ and q is known as the *Brody* or *repulsion parameter*. Interpolation between the two extremes is governed by the value of q: the Poisson-Wigner distributions are recovered when $q = 0$ or 1, respectively. A value of $q = 0.50$ therefore indicates a degree of level repulsion somewhere intermediate between that of Poisson (no repulsion) and Wigner. Such behavior has been observed for numerous ionic systems in the past. For example, Connerade *et al.* [38] have obtained a value of $q = 0.59$ for the $4p$ spectrum of strontium. The current task is now to evaluate the Brody parameter for the four interacting sets considered in the present work.

There exists various methods in the literature for computing the Brody parameter q. In this study, we will restrict ourselves to the T-function approach of Robnik and Prozen [38–40]. First, we define the *cumulative spacing distribution*, $\Pi(s)$, as

$$\Pi(s) = \frac{1}{(n-1)} \sum_{i=1}^{n-1} \Theta(s - s_i), \tag{14}$$

where n is the number of energy levels. Effectively, $\Pi(s)$ is the number of adjacent level pairs separated by a spacing of at most s divided by the total number of spacings in the interacting set. This quantity is shown in Figs. 10 and 11 for the $J^\pi = 7/2^-$ and 4^+ interacting sets, respectively. For both sets, the majority of spacings take on values in the range $0.1 \leqslant s \leqslant 2$. Relatively few spacings exist for $s > 2$, the most extreme case being $s = 3.43$ in the $J^\pi = 7/2^-$ set.

TABLE III. Parameters ρ_0 and a of Eq. (12) used to unfold the level spectra of the $J^\pi = 4^+$ (No XIII) and $J^\pi = 3^+$ (Md XIV) interacting sets [these parameters do not apply for the $J^\pi = 3^+$ (Bk XII) and $J^\pi = \frac{7}{2}^-$ (Cf XII) sets as a straight line fit was used]. The 95% confidence bounds (C.B.) of the fits and the corresponding Brody parameters q associated with each ion stage are also tabulated.

J^π	Ion stage	ρ_0 (eV^{-1})	a (eV$^{-1/2}$)	C.B. (95%)	q
3^+	Bk XII			± 0.037	0.659
$\frac{7}{2}^-$	Cf XII			± 0.017	0.977
4^+	No XIII	0.144	1.001	± 0.036	0.863
3^+	Md XIV	0.164	0.8424	± 0.041	0.952

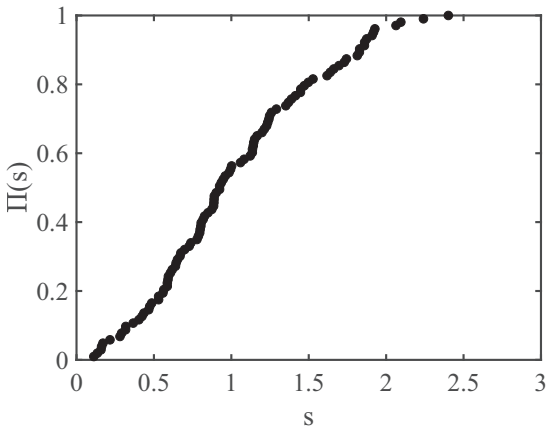

FIG. 11. Cumulative spacing distribution $\Pi(s)$ as a function of NNS's s for the $J^\pi = 4^+$ interacting set in No XIII.

Now, supposing that the spacings are distributed according to the Brody distribution, we can write that

$$\Pi(s) = \int_0^s P(s')ds'. \tag{15}$$

Inserting (13) into (15) and making the substitution $u = (s')^{q+1}$, an explicit dependence of $\Pi(s)$ on q is obtained:

$$\Pi(s) = 1 - \exp(-\alpha s^{q+1}) \tag{16}$$

Using this expression, Robnik and Prozen [39] introduced the so-called T function $T(s) \equiv \ln(\ln((1-\Pi(s))^{-1}))$. Interestingly, this function transforms the Brody distribution (13) into a straight line via

$$T(s) = \ln(\alpha) + (1+q)\ln(s). \tag{17}$$

The parameter q can be obtained from the slope $(1+q)$ of the line of best fit to $T(s)$. The results are shown in Figs. 12 and 13 for the two interacting sets considered previously. Shown also in these figures are the $\pm$ one sigma errors on the T function, $\delta T(s)$, which have been calculated using [39]

$$\delta T(s) = \frac{\sqrt{\Pi(s)}}{\sqrt{(n-1)[1-\Pi(s)]|\ln[1-\Pi(s)]|}}. \tag{18}$$

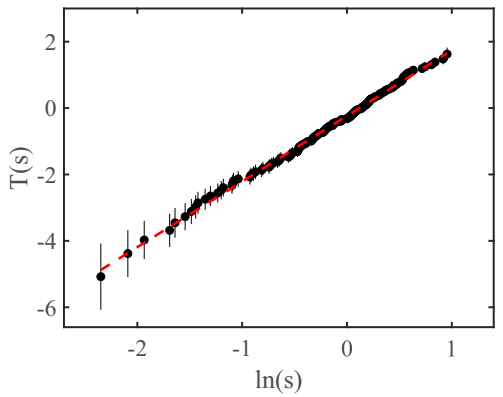

FIG. 12. $T(s)$ as a function of $\ln(s)$ for the $J^\pi = 7/2^-$ interacting set in Cf XII. The line of best fit is shown in red.

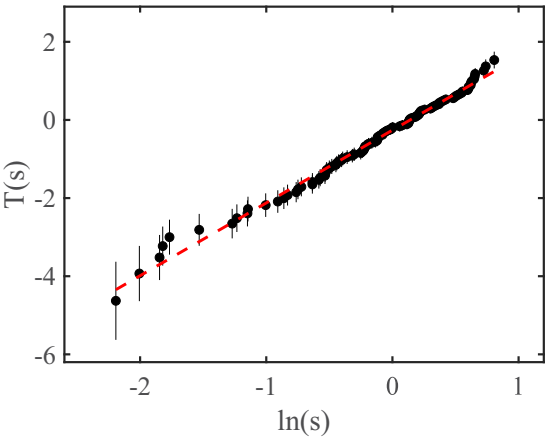

FIG. 13. $T(s)$ as a function of $\ln(s)$ for the $J^\pi = 4^+$ interacting set in No XIII. The line of best fit is shown in red.

In both cases, the lines of best fit reproduce the data quite well. Brody parameters q associated with the four interacting sets are presented in Table III. Three of the interacting sets (Cf XII, No XIII, and Md XIV) demonstrate strong level repulsion, as illustrated by values of $q = 0.977$, 0.863, and 0.952, respectively. A value of $q = 0.659$ for the $J^\pi = 3^+$ set in Bk XII demonstrates intermediate behavior. The 95% confidence bounds for the fits are also tabulated, and these values indicate small errors on the calculated q values. In Figs. 14 and 15 we have plotted histograms of the spacing distributions for these two sets. The plots clearly illustrate good fits of the Brody distributions to the data, which is reinforced by values of $\chi^2(13) = 0.21$ and $\chi^2(8) = 0.04$, both of which are above the respective 99.95% confidence levels.

Although the T-function approach does allow for the accurate determination of q, it does exhibit some undesirable features. One of these features is the existence of spacing-dependent errors. From Figs. 12 and 13, one can see that the errors on $T(s)$ increase as one moves to smaller values of s. Another drawback of this function is that it gives a nonuniform distribution of $T(s)$ values across the entire spacing range. The data point density clearly increases as one

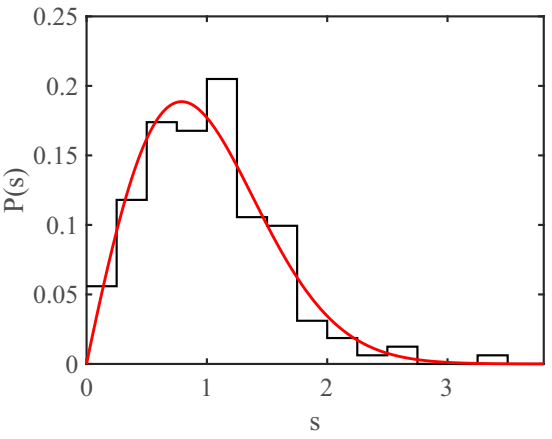

FIG. 14. Distribution of NNS's for the $J^\pi = 7/2^-$ interacting set in Cf XII. A Brody distribution with $q = 0.977$ is shown in red.

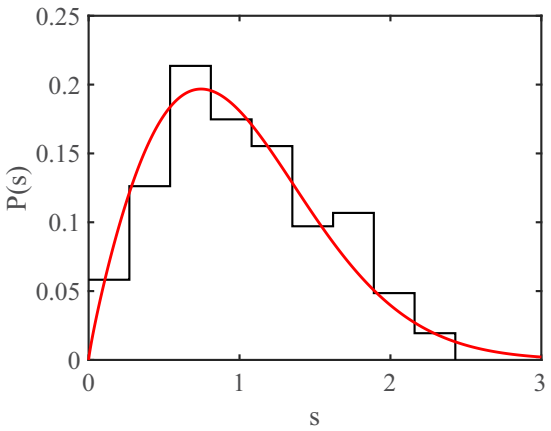

FIG. 15. Distribution of NNS's for the $J^\pi = 4^+$ interacting set in No XIII. A Brody distribution with $q = 0.863$ is shown in red.

moves to larger values of s, resulting in more information being located at larger $\ln(s)$ values [39]. In order to overcome these drawbacks, in the same study, Robnik and Prozen [39] introduced the so-called U function, defined as

$$U(\Pi(s)) = \frac{2}{\pi}\arccos[\sqrt{1-\Pi(s)}]. \tag{19}$$

Importantly, this function exhibits a constant error $\delta U = 1/[\pi\sqrt{(n-1)}]$ for all spacings. We have used this function to determine the accuracy of the Brody distribution in describing the FAC-calculated level distributions for the two test cases of $J^\pi = 7/2^-$ and 4^+. First, we calculated $U(\Pi(s))$ using values of $\Pi(s)$ plotted in Figs. 10 and 11. Then, using Eq. (16) and a value of q obtained from the T-function approach, the "Brody-predicted" U function, $U_q(\Pi(s))$, was calculated. The accuracy of this function was then tested by plotting the difference $U(\Pi(s)) - U_q(\Pi(s))$. The results for the two test cases are shown in Figs. 16 and 17. The bold lines represent the two quantities $U(\Pi(s)) - U_q(\Pi(s)) \pm \delta U$ and the dashed lines simply connect the two "extreme" points, illustrating the range of possible intermediate values. Both plots illustrate the high accuracy to which the Brody-predicted U function reflects the true U function. Indeed, maximum deviations of

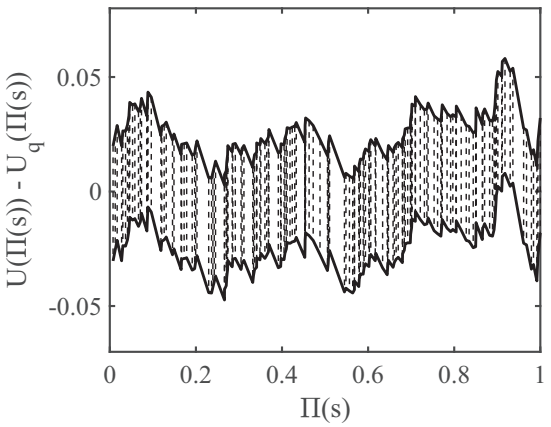

FIG. 16. Quantity $U(\Pi(s)) - U_q(\Pi(s)) \pm \delta U$ as a function of $\Pi(s)$ for the $J^\pi = 7/2^-$ interacting set.

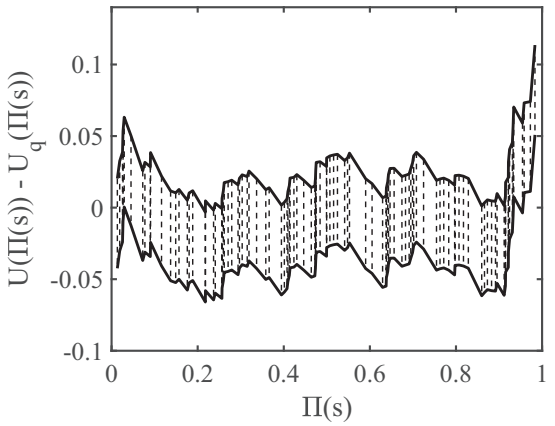

FIG. 17. Quantity $U(\Pi(s)) - U_q(\Pi(s)) \pm \delta U$ as a function of $\Pi(s)$ for the $J^\pi = 4^+$ interacting set.

0.058 and 0.115 are observed for the $J^\pi = 7/2^-$ and 4^+ interacting sets, respectively.

D. Covariance of adjacent spacings

A statistical measure often used in the study of short-range correlations is the *covariance of adjacent spacings*, $\mathrm{cov}(s_i, s_{i+1})$, given by [8]

$$\begin{aligned}\mathrm{cov}(s_i, s_{i+1}) &= \left[\sum_{i=1}^{n-2}(s_i - \langle s_i\rangle)(s_{i+1} - \langle s_{i+1}\rangle)\right] \\ &\times \left[\left(\sum_{i=1}^{n-2}(s_i - \langle s_i\rangle)^2\right)\left(\sum_{i=1}^{n-2}(s_{i+1} - \langle s_{i+1}\rangle)^2\right)\right]^{-1/2}\end{aligned} \tag{20}$$

This statistic measures correlations between levels ϵ_i and ϵ_{i+2} and is predicted by GOE theory to have a value of $\mathrm{cov}(s_i, s_{i+1}) = -0.27$. We have calculated this statistic for the four interacting sets, the results of which are presented in Table IV. For these calculations, we assume a mean level spacing of 1, i.e., we have taken $\langle s_i\rangle = \langle s_{i+1}\rangle = 1$. The results obtained for the $J^\pi = 7/2^-$ and 4^+ sets are clearly in very good agreement with the GOE-predicted value. Larger deviations from the GOE-predicted value are observed for the $J^\pi = 3^+$ sets in Bk XII and Md XIV (0.0459 and 0.1057, respectively).

TABLE IV. Covariance of adjacent spacings $\mathrm{cov}(s_i, s_{i+1})$ and the interval bounds $[a, b]$ and corresponding $L_{\max}$ values used in the calculation of $\langle\Delta_3(L)\rangle$ for the four interacting sets.

J^π	Ion stage	$\mathrm{cov}(s_i, s_{i+1})$	a	b	$L_{\max}$
3^+	Bk XII	−0.3159	10	90	40
$\frac{7}{2}^-$	Cf XII	−0.2611	20	140	60
4^+	No XIII	−0.2541	10	90	40
3^+	Md XIV	−0.3757	10	80	35

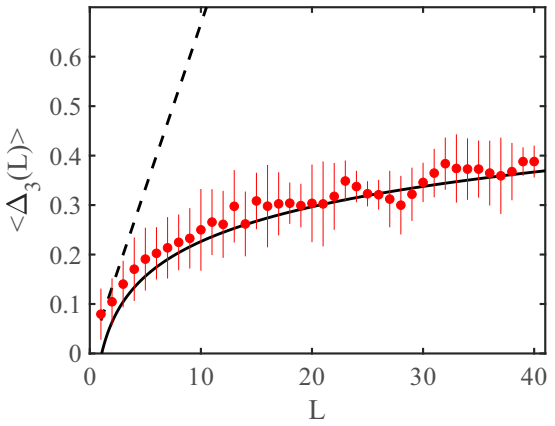

FIG. 18. Variation of $\langle\Delta_3(L)\rangle$ with L for the $J^\pi = 3^+$ interacting set in Bk XII. The broken and solid curves correspond to $\Delta_{3,\text{Poisson}}(L)$ and $\Delta_{3,\text{Wigner}}(L)$, respectively (see text).

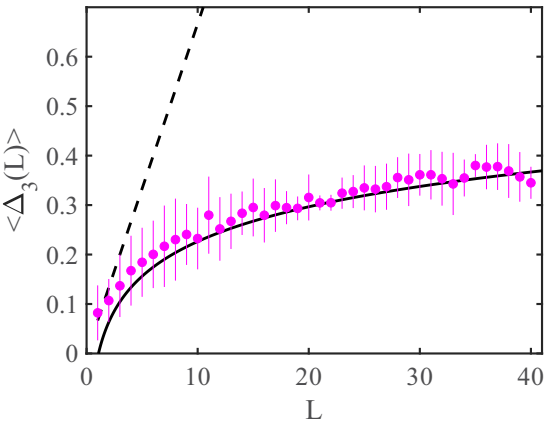

FIG. 20. Variation of $\langle\Delta_3(L)\rangle$ with L for the $J^\pi = 4^+$ interacting set in No XIII. The broken and solid curves correspond to $\Delta_{3,\text{Poisson}}(L)$ and $\Delta_{3,\text{Wigner}}(L)$, respectively (see text).

E. Dyson-Mehta statistic

Thus far, we have investigated the existence of short-range correlations in the spectrum using the Brody distribution and the covariance of adjacent spacings. However, these quantities provide no insight into the existence of long-range correlations in the level spectrum. In this section, we wish to investigate the role, if any, that long-range correlations play in the formation of the observed level structures.

A standard measure of long-range correlations, utilized extensively in nuclear physics, is the *Dyson-Mehta statistic* or *spectral rigidity* $\Delta_3(L)$ [41]. In order to describe this measure, recall Fig. 8 where we have plotted a subsection of the mode number as a function of unfolded energies for the $J^\pi = 7/2^-$ interacting set. Shown in red is the line of best fit. The Dyson-Mehta statistic, $\Delta_3(L)$, quantifies the fluctuations of the mode number, $N(E)$, from this line of best fit. This statistic measures the root-mean-squared deviation of $N(E)$ from the best fit line. Mathematically, $\Delta_3(L)$ is defined for the interval $[a, a + L]$ as

$$\Delta_3(a, L) = \frac{1}{L} \min_{A,B} \int_a^{a+L} [N(x) - (Ax + B)]^2 dx, \qquad (21)$$

where A and B represent the coefficients of the best-fit line. This quantity has been evaluated for the four interacting sets considered in the present work. We have adopted the method outlined in [42–44] for the calculation of $\Delta_3(L)$. First, Eq. (21) is rewritten in the form [42]

$$\Delta_3(a, L) = \frac{M^2}{16} - \frac{1}{L^2}\left[\sum_{i=1}^{M} \tilde{x}_i\right]^2 + \frac{3M}{2L^2}\left[\sum_{i=1}^{M} \tilde{x}_i^2\right] - \frac{3}{L^4}\left[\sum_{i=1}^{M} \tilde{x}_i^2\right]^2 + \frac{1}{L}\left[\sum_{i=1}^{M} (M - 2i + 1)\tilde{x}_i\right], \qquad (22)$$

where $\tilde{x}_i = x_i - (a + L/2)$ and M is the number of x_i in the interval $[a, a + L]$. We then proceed as described in [43,44], where we calculate $\Delta_3(L)$ for numerous overlapping intervals, and then average the final results in a process known

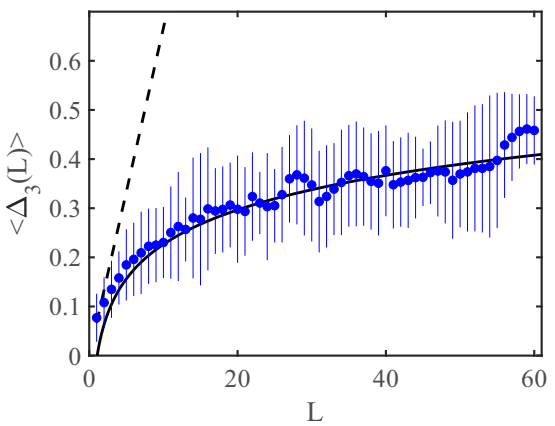

FIG. 19. Variation of $\langle\Delta_3(L)\rangle$ with L for the $J^\pi = 7/2^-$ interacting set in Cf XII. The broken and solid curves correspond to $\Delta_{3,\text{Poisson}}(L)$ and $\Delta_{3,\text{Wigner}}(L)$, respectively (see text).

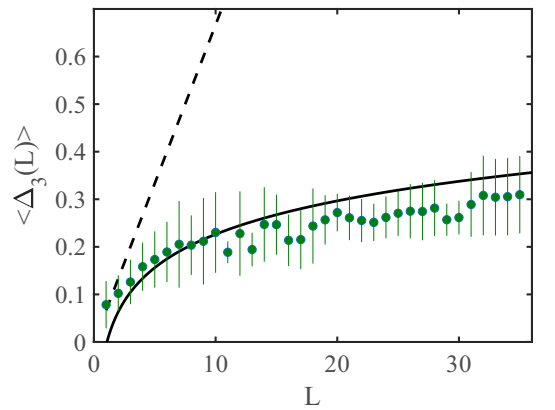

FIG. 21. Variation of $\langle\Delta_3(L)\rangle$ with L for the $J^\pi = 3^+$ interacting set in Md XIV. The broken and solid curves correspond to $\Delta_{3,\text{Poisson}}(L)$ and $\Delta_{3,\text{Wigner}}(L)$, respectively (see text).

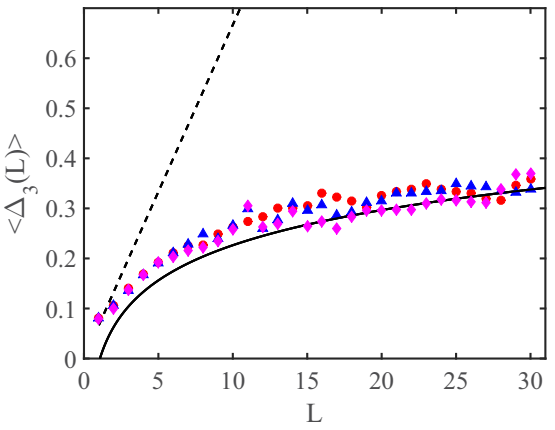

FIG. 22. Variation of $\langle\Delta_3(L)\rangle$ with L for the $J^\pi = 3^+$ interacting set in Bk XII. The red circles, blue triangles, and magenta diamonds correspond to the intervals $[a, b] = [10, 70]$, $[20, 80]$, and $[30, 90]$, respectively. The broken and solid curves correspond to $\Delta_{3,\text{Poisson}}(L)$ and $\Delta_{3,\text{Wigner}}(L)$, respectively (see text).

as *spectral averaging*. More specifically, choosing an interval $[a, b]$ on the unfolded energy scale, we calculate $\Delta_3(L)$ for the intervals $[a, a + L]$, $[a + L/2, a + 3L/2]$, $[a + L, a + 2L]$, $[a + 3L/2, a + 5L/2], \ldots$, until the range $[a, b]$ has been covered. We then average the results to obtain $\langle\Delta_3(L)\rangle$. However, in this method, it is important to note that, for any choice of L, the final overlapping interval will actually extend beyond the upper limit b. In this sense, the final interval should not be included in the averaging process, as its length differs from the other intervals. Care must be taken when choosing large values of L, as certain intervals $[a, b]$ may only accommodate 1 or 2 true intervals of length L. Therefore, it is best practice to choose a significantly large interval $[a, b]$ over which to compute $\langle\Delta_3(L)\rangle$. For example, in the case of Bk XII, the unfolded energy interval extends from -1.8355 to 107.8787. Choosing the interval $[a, b] = [10, 90]$ results in three adjacent overlapping intervals for a value of $L = 40$. The minimum number of overlapping intervals considered in the present work is 3, and this fixes the maximum value of L for a given set. The interval ranges $[a, b]$ and maximum values of L, "$L_{\max}$," associated with each interacting set are provided in Table IV.

For a system whose levels are distributed randomly according to the Poisson distribution, the $\Delta_3(L)$ statistic has a soft character and exhibits a linear dependence on interval length $[\Delta_{3,Poisson}(L) = L/15]$. On the other hand, a system which conforms to GOE statistics upholds a much stronger rigidity in its level structure, owing to the highly correlated, repulsive nature of its eigenvalues. In these systems, the $\Delta_3(L)$ statistic exhibits a slowly varying, logarithmic dependence on the interval length $(\Delta_{3,\text{Wigner}}(L) = \pi^{-2}[\ln(L) - 0.0686])$. In Figs. 18–21 we have plotted $\Delta_{3,Poisson}(L)$ (dashed line) and $\Delta_{3,Wigner}(L)$ (full line) along with the quantity $\langle\Delta_3(L)\rangle$ for each interacting set. The vertical lines associated with each $\langle\Delta_3(L)\rangle$ value correspond to $\pm$ one standard deviation σ obtained from the averaging process. From these figures, one can see overwhelming evidence of GOE-like behavior in the $\langle\Delta_3(L)\rangle$ statistic for each of the four sets. The $J^\pi = 3^+, 4^+$ interacting sets in Bk XII and No XIII show very similar behavior, with the latter perhaps exhibiting smaller $\pm\sigma$ values than the former. Although the $J^\pi = 7/2^-$ group does follow the general trend set down by $\Delta_{3,\text{Wigner}}(L)$, this group clearly shows much larger $\pm\sigma$ values than any of the other interacting sets. It is interesting to note that, for $L \leqslant 10$, the $\langle\Delta_3(L)\rangle$ quantity follows a similar behavior for all sets. However, examining the $J^\pi = 3^+$ set at values $L > 10$, it appears that this level structure displays a more pronounced rigidity than the other sets, evident from $\langle\Delta_3(L)\rangle \pm \sigma$ generally lying below that of the other sets.

Finally, it is important to note that, if the spectrum fluctuations are translationally invariant, then, as highlighted in [44], $\langle\Delta_3(L)\rangle$ will be independent of the chosen interval $[a, b]$. This can be tested by shifting the interval $[a, b]$ along the unfolded axis and comparing values of $\langle\Delta_3(L)\rangle$ calculated for different intervals. To test this, we have considered once again the $J^\pi = 3^+$ interacting set in Bk XII and have calculated values for $\langle\Delta_3(L)\rangle$ using the three intervals $[a, b] = [10, 70]$, $[20, 80]$, and $[30, 90]$. The results are shown in Fig. 22. Clearly, the three data sets show similar calculated values for $\langle\Delta_3(L)\rangle$. Although the $\pm\sigma$ bars have been omitted for clarity, their inclusion would highlight significant overlap in the range of allowed $\langle\Delta_3(L)\rangle$ values, defined by $\pm\sigma$, for each of the three data sets. Therefore, within the $\pm\sigma$ bounds, this plot demonstrates the existence of translationally invariant spectrum fluctuations over the three intervals $[a, b] = [10, 70]$, $[20, 80]$, and $[30, 90]$.

IV. CONCLUSIONS

In the present study, we have identified the existence of many-body quantum chaotic features in the energy-level spectra of four high-Z, moderately charged actinide ions. This has been made possible through a RMT statistical analysis of the level sequences. The existence of short- and long-range correlations in the level spectra has been identified through evaluation of quantities such as the repulsion parameter q, the covariance of adjacent spacings $\text{cov}(s_i, s_{i+1})$, and the Dyson-Mehta statistic $\Delta_3(L)$. The results of these calculations are in very good agreement with RMT predictions. This study therefore extends the identification of many-body quantum chaos to high-Z actinide ions.

ACKNOWLEDGMENTS

J.S. acknowledges funding from the Irish Research Council (Grant No. GOIPG/2015/3756). J.S. would like to thank G. O'Sullivan and D. Kilbane for useful discussions and their assistance in the preparation and presentation of the manuscript. J.S. would also like to thank the anonymous referee for useful comments and suggestions.

[1] V. Plerou, P. Gopikrishnan, B. Rosenow, L. A. N. Amaral, T. Guhr, and H. E. Stanley, Phys. Rev. E **65**, 066126 (2002).

[2] C. Ellegaard, T. Guhr, K. Lindemann, H. Q. Lorensen, J. Nygård, and M. Oxborrow, Phys. Rev. Lett. **75**, 1546 (1995).

[3] C. Ellegaard, T. Guhr, K. Lindemann, J. Nygård, and M. Oxborrow, Phys. Rev. Lett. **77**, 4918 (1996).
[4] D. Kilbane, A. Cummings, D. M. Heffernan, and G. O'Sullivan, Phys. Scr. **73**, 198 (2006).
[5] C. E. Porter, *Statistical Theories of Spectra: Fluctuations* (Academic, New York, 1965).
[6] F. Kahn, H. S. Camarda, G. Hacken, W. W. Havens, Jr., H. I. Liou, J. Rainwater, M. Slagowitz, and S. Wynchank, Phys. Rev. C **6**, 1854 (1972).
[7] F. J. Dyson, J. Math. Phys. **3**, 157 (1962).
[8] M. L. Mehta, *Random Matrices*, 3rd ed. (Academic Press, New York, 2004).
[9] H. I. Liou, H. S. Camarda, S. Wynchank, M. Slagowitz, G. Hacken, F. Rahn, and J. Rainwater, Phys. Rev. C **5**, 974 (1972).
[10] F. J. Dyson, J. Math. Phys. **3**, 140 (1962).
[11] N. Rosenzweig and C. E. Porter, Phys. Rev. **120**, 1698 (1960).
[12] H. S. Camarda and P. D. Georgopulos, Phys. Rev. Lett. **50**, 492 (1983).
[13] W. C. Martin, R. Zalubas, and L. Hagan, *NSRDS-NBS* (National Bureau of Standards, Washington, DC, 1978).
[14] V. V. Flambaum, A. A. Gribakina, G. F. Gribakin, and M. G. Kozlov, Phys. Rev. A **50**, 267 (1994).
[15] B. V. Chirikov, Phys. Lett. A **108**, 68 (1985).
[16] G. O'Sullivan, P. K. Carroll, P. Dunne, R. Faulkner, C. McGuinness, and N. Murphy, J. Phys. B **32**, 1893 (1999).
[17] D. Kilbane, A. Cummings, C. McGuinness, N. Murphy, and G. O'Sullivan, J. Phys. B **35**, 309 (2002).
[18] M. G. Mayer, Phys. Rev. **60**, 184 (1941).
[19] T. Y. Wu, Phys. Rev. **44**, 727 (1933).
[20] A. R. P. Rao and U. Fano, Phys. Rev. **167**, 7 (1968).
[21] J. P. Connerade and M. W. D. Mansfield, Phys. Rev. Lett. **48**, 131 (1982).
[22] A. Cummings, C. McGuinness, G. O'Sullivan, J. T. Costello, J. P. Mosnier, and E. T. Kennedy, Phys. Rev. A **63**, 022702 (2001).
[23] P. K. Carroll and G. O'Sullivan, Phys. Rev. A **25**, 275 (1982).
[24] G. O'Sullivan, J. Phys. B **16**, 3291 (1983).
[25] D. Kilbane and G. O'Sullivan, Phys. Rev. A **82**, 062504 (2010).
[26] A. V. Viatkina, M. G. Kozlov, and V. V. Flambaum, Phys. Rev. A **95**, 022503 (2017).
[27] J. Sheil, D. Kilbane, G. O'Sullivan, L. Liu, and C. Suzuki, Phys. Rev. A **96**, 062501 (2017).
[28] M. F. Gu, Can. J. Phys. **86**, 675 (2008).
[29] A. Bar-Shalom, M. Klapisch, and J. Oreg, J. Quant. Spectrosc. Radiat. Transfer **71**, 169 (2001).
[30] D. H. Sampson, H. L. Zhang, A. K. Mohanty, and R. E. H. Clark, Phys. Rev. A **40**, 604 (1989).
[31] H. L. Zhang, D. H. Sampson, and A. K. Mohanty, Phys. Rev. A **40**, 616 (1989).
[32] R. D. Cowan, *The Theory of Atomic Structure and Spectra* (University of California Press, Berkeley, 1981).
[33] M. G. Kozlov, S. G. Porsev, and I. I. Tupitsyn, arXiv:physics/0004076.
[34] A. Bohr and B. Mottelson, *Nuclear Structure, Volume I: Single-Particle Motion* (Benjamin, New York, 1969).
[35] V. V. Flambaum, A. A. Gribakina, and G. F. Gribakin, Phys. Rev. A **58**, 230 (1998).
[36] T. A. Brody, J. Flores, J. B. French, P. A. Mello, A. Pandey, and S. S. M. Wong, Rev. Mod. Phys. **53**, 385 (1981).
[37] J. P. Connerade, *Highly Excited Atoms* (Cambridge University Press, Cambridge, UK, 1998).
[38] J. P. Connerade, I. P. Grant, P. Marketos, and J. Oberdisse, J. Phys. B **28**, 2539 (1995).
[39] T. Prozen and M. Robnik, J. Phys. A: Math Gen. **26**, 2371 (1993).
[40] K. Ganesan and M. Lakshmanan, J. Phys. B **27**, 2809 (1994).
[41] F. J. Dyson and M. L. Mehta, J. Math. Phys. **4**, 701 (1963).
[42] O. Bohigas and M. J. Giannoni, Ann. Phys. (N.Y.) **89**, 393 (1975).
[43] W. E. Ormand and R. A. Broglia, Phys. Rev. C **46**, 1710 (1992).
[44] O. Bohigas, M. J. Giannoni, and C. Schmit, Phys. Rev. Lett. **52**, 1 (1984).